PCCP

Accepted Manuscript

ROYAL SOCIETY OF CHEMISTRY

www.rsc.org/pccp

Structures and Energies of Cu Clusters on Fe and Fe_3C Surfaces from Density Functional Theory Computation

Xinxin Tian,[a,b,c] Tao Wang,[d] Yong Yang,[a,b] Yong-Wang Li,[a,b] Jianguo Wang,[a] Haijun Jiao*,[a,d]

a) State Key Laboratory of Coal Conversion, Institute of Coal Chemistry, Chinese Academy of Sciences, Taiyuan,030001, China; b) National Energy Center for Coal to Liquids, Synfuels CHINA Co., Ltd, Huairou District, Beijing, 101400, China; c) University of Chinese Academy of Sciences, Beijing, 100049, China; d) Leibniz-Institut für Katalyse eV., an der Universität Rostock, Albert-Einstein-Strasse 29a, 18059 Rostock, Germany. E-mail address: haijun.jiao@catalysis.de

Abstract

Spin-polarized density functional theory computations have been carried out to study the stable adsorption configurations of Cu_n (n = 1-7, 13) on Fe and Fe_3C surfaces for understanding the initial stages of copper promotion in catalysis. At low coverage, two-dimensional aggregation is more preferred over dispersion and three-dimensional aggregation on the Fe(110) and Fe(100) as well as the metallic $Fe_3C(010)$ surfaces, while dispersion is more favorable over aggregation on the Fe(111) surface. On the $Fe_3C(001)$ and $Fe_3C(100)$ surfaces with exposed iron and carbon atoms, the adsorbed Cu atoms prefer dispersion at low coverage, while aggregation along the iron regions at high coverage. On the iron surfaces, the adsorption energies for Cu_n (n = 2-7) are highest on Fe(111), medium on Fe(100) and lowest on Fe(110). On the Fe_3C surfaces, the adsorption energies for Cu_n (n = 1-3) are highest on $Fe_3C(100)$, medium on $Fe_3C(010)$ and lowest on $Fe_3C(001)$, while, for n = 4-7 and 13, $Fe_3C(010)$ has stronger adsorption than $Fe_3C(100)$. On the basis of their differences in electronegativity, the adsorbed Cu atoms can oxidize the metallic Fe(110), Fe(100) and $Fe_3C(010)$ surfaces and become negatively charged. On the $Fe_3C(001)$ and $Fe_3C(100)$ surfaces with exposed iron and carbon atoms, the adsorbed Cu atoms interacting with surface carbon atoms are oxidized and positively charged. Unlike the most stable Fe(110) and $Fe_3C(001)$ surfaces, where the Fe(110) surface has stronger Cu affinity than the $Fe_3C(001)$ surface, which is in agreement with the experimental finding, the less and least stable $Fe_3C(010)$ and $Fe_3C(100)$ surfaces have stronger Cu affinities than the Fe(110) and Fe(100) surfaces. Since less stable facts are not preferably formed thermodynamically, it is crucial to prepare such surfaces to explore Cu adsorption and promotion, and this provides challenges to surface sciences.

1. Introduction

Fischer-Tropsch synthesis (FTS, $CO + H_2 \rightarrow C_xH_y + H_2O + CO_2$)[1-3] is an enabling technology in converting synthesis gas from coal, natural gas and biomass into transport fuels and value-added chemicals. Suitable FTS catalysts for industrial applications are iron- and cobalt-based,[4-6] but iron-based catalysts become dominant due to lower costs. Initial Fe-based FTS catalysts are generally hematite (α-Fe_2O_3) and have to be reduced before becoming active. During the reduction, α-Fe_2O_3 is firstly reduced to magnetite (Fe_3O_4) by using H_2, synthesis gas or CO and further to phases consisting of metallic iron, iron oxides and iron carbides in varying proportions depending on preparation conditions.[7-9] Several iron carbide phases (ε-Fe_2C, χ-Fe_5C_2, θ-Fe_3C and Fe_7C_3) have been detected experimentally.[10] Apart from Fe_5C_2, the Fe_3C phase is also active in FTS.[11,12]

Practically iron-based FTS catalysts consist of not only pure iron components (metallic iron, iron oxides and iron carbides) but also promoters such as copper, potassium and silica or zinc oxide. The role of copper in Fe-based FTS has attracted considerable attention and has been extensively studied experimentally.[13] Copper has been found to facilitate Fe_3O_4 conversion to metallic iron[14] and to lower the reduction temperature.[15] Under H_2, de Smit *et al.*,[16] found that Cu-promoted catalysts can be easier reduced at low temperature than un-promoted catalysts at high temperature, while they did not observe such difference under synthesis gas. Recently, copper has been reported to suppress the χ-Fe_5C_2 phase formation under CO.[17,18] Copper can promote carburization rate,[19-21] increase the activities of FTS and water-gas shift (WGS, $CO + H_2O \rightarrow CO_2 + H_2$) reaction[22-25] and synergistic effect was observed on copper and potassium co-promoted catalyst.[26] However, controversial observations about Cu-promotion on hydrocarbon selectivity in FTS were reported.[15,19,22,26]

Experimentally, the structures of Cu species in promoted catalysts are difficult to image due to the rather low content and very high dispersion. A previous study in characterizing the surface of Fe and Fe-Cu FTS catalysts by Wachs *et al*.,[27] showed that Cu agglomerates on the reduced iron surface and exhibits even lower affinity on the carburized iron surface; and additional agglomeration occurs when the catalysts are exposed to H_2/CO environment. A recent synchrotron-based *in situ* X-ray photoelectron spectroscopy study on the surface of Cu-promoted Fe-based FTS catalyst[28] showed that the reduced Cu species spreads to the metallic Fe surface of either supported catalyst or un-supported catalyst when treated at 275°C. When treated at 350°C, however, Cu phases agglomerate and move to the support surface. In addition, Cu quantity was found to affect FTS activities. For example, Ma *et al*.,[29] found that Cu content up to 2.0 wt% enhances iron reduction significantly but lowers the activities of FTS and WGS. In investigating the Cu modified Al_2O_3 as support in Fe-based FTS catalysts, Pansanga *et al*.,[30] found higher activity for catalysts supported on 10 wt.% Cu modified Al_2O_3 than those modified with only 1 wt.% Cu. Wielers *et al*.,[31] found that Cu content does not affect the product selectivity within a broad range (< 60 at. % Cu), while catalyst with 10-20 at. % Cu has the highest FTS activity. In studying the effect of Cu content on the bifunctional Fe-Cu-K/ZSM5 catalyst Bae *et al*.,[32] found a Cu optimum (2 wt.%) for the activity, while higher Cu content results in iron oxide segregation which eventually lowers the catalytic performances. It is reported that Cu content less than 0.1 wt% is sufficient to produce an active FTS catalyst.[33] In addition, the promotion effect of Au on Fe(111), Ag and Cu on Fe(100) surfaces in ammonia synthesis has been investigated, the promoter species were deposited by evaporation from a source consisting of a high purity Au/Ag/Cu wire wrapped around a resistively heated W wire.[34]

In contrast to these intensive and extensive experimental studies, there are only few theoretical reports about Cu promotion on Fe-based FTS catalysts. For instance, CO adsorption and dissociation as well as C-C coupling based on Fe/Cu surface alloy model[35] and monolayer Cu adsorbed model on Fe surface[36] were previously investigated. Zhao *et al*.,[37] studied CO dissociation on bimetallic Cu/Fe catalyst and found that Cu doping can reduce CO dissociation activity. In order to explore Cu promotion in CO activation, Tian *et al*.,[38] studied CO adsorption and dissociation on the clean as well as *n*Cu-adsorbed and *n*Cu-substituted Fe(100) surfaces (*n* = 1-3) at different coverage. It is found that increasing Cu content not only weakens CO adsorption but also increases CO dissociation barriers as well as make CO dissociation thermodynamically less favorable, and the clean Fe(100) sur-

face is most active in CO adsorption and dissociation. The *n*Cu-substituted Fe(100) surface can suppress CO adsorption and dissociation more strongly than the *n*Cu-adsorbed Fe(100) surface. Our previous work on Cu_n adsorption on the most stable Fe(110) and $Fe_3C(001)$ surfaces[39] found that Cu_n favor aggregation on Fe(110) and dispersion on $Fe_3C(001)$ at low Cu content, while favor monolayer structure on both surfaces at high Cu content. Furthermore, Fe(110) has stronger Cu affinity than $Fe_3C(001)$, in agreement with the experimental observation. To our knowledge, no reports about Cu phases on other metallic iron or iron carbide surfaces are available. Since each stable and active catalyst can have more than one exposed facets having different stabilities and activities as well as jointly determining the whole catalytic performance, we examined the structures and energies of Cu_n (*n* = 1-7; 13) adsorption on the less and least stable Fe(100) and Fe(111) as well as $Fe_3C(100)$ and $Fe_3C(010)$ surfaces to give more detailed structural and energetic understanding into Cu adsorption on Fe-based FTS catalysts. Our results provide some references for advanced experimental studies and a rational model for discussing Cu promotion, which is of pronounced importance for understanding Fe-based FTS mechanisms.

2. Computational details

2.1. Methods: All calculations were performed at the level of density functional theory within the Vienna Ab initio Simulation Package (VASP).[40,41] The projected augmented wave method (PAW)[42] and the generalized gradient approximation (GGA)[43] were used. The exchange and correlation energies were calculated using the Perdew-Burke-Ernzerhof (PBE) functional.[44] The cutoff energy of 400 eV was used throughout this study. Spin-polarization calculation was included for iron systems to correctly account for the magnetic properties. Geometry optimization was done when atomic force tolerance becomes smaller than 0.02 eV/Å and the energy difference was lower than 10^{-4} eV. Bader charge analysis[45] was carried out for discussing charge transfer between the surface and the adsorbed Cu atoms. Transition states were estimated using the climbing-image nudged elastic band (CI-NEB) method.[46,47] Vibrational frequencies were also calculated.

Adsorption energies, stepwise adsorption energies and aggregation energies are used to describe the properties of Cu_n on the surfaces. For Cu_n adsorption on the surface, the total adsorption energy [$E(Cu_{n/ads})$] is defined according to equation 1 and the average adsorption energy [$E(Cu_{ads/av}$] is given in equation 2, where $E(Cu)_n$/slab is the total energy of the slab with the adsorbed Cu_n species, E(slab) is the total energy of the clean slab and n is the number of the adsorbed Cu atoms, and $E(Cu_{gas})$ is the total energy of an isolated Cu atom in gas phase.

$$E(Cu_{n/ads}) = [E(Cu)_n/\text{slab} - E(\text{slab}) - nE(Cu_{gas})] \quad \text{Eq. 1}$$

$$E(Cu_{ads/av}) = E(Cu_{n/ads})/n \quad \text{Eq. 2}$$

The stepwise adsorption energy [$\Delta E(Cu_{ads})$] is defined according to equation 3.

$$\Delta E(Cu_{ads}) = E(Cu_{n/ads}) - E(Cu_{n-1/ads}) \quad \text{Eq. 3}$$

In addition, we defined the average aggregation energy [$E_{agg}(Cu_{ads})$] of surface Cu_n in equation 4; and a larger (more negative) aggregation energy means a stronger Cu_n adsorption. It should be noted that surface Cu_n in this study means n-numbered Cu atoms, because when n-numbered Cu atoms adsorbed on the surfaces, both Cu_n clusters and *n*-dispersed Cu atoms on surfaces might be stable thermodynamically.

$$E_{agg}(Cu_{ads}) = [E(Cu_{n/ads}) - nE(Cu_{1/ads})]/n \quad \text{Eq. 4}$$

We also defined the stepwise growth energy according to equation 5; and the larger (more negative) the stepwise growth energy [$E_{growth}(Cu_{ads})$] of $Cu_{n/ads}$, the stronger the aggregation ability of Cu_{n-1} to get one more Cu atom on the surface.

$$E_{growth}(Cu_{ads}) = E(Cu_{n/ads}) - E(Cu_{n-1/ads}) - E(Cu_{ads}) \quad \text{Eq. 5.}$$

It is noted that in our computation we used Cu atom to study the adsorption energies as well as aggregation energies in gas phase and on surface; and our idea comes from the experimental observation of the adsorption of Au on Fe(111), Ag and Cu on Fe(100) surfaces from evaporation in investigating promotion effect in ammonia synthesis.[34] In addition, for studying the role of

iron loading and potassium and cupper promoters, the synthesis and characterization of nano-iron carbides using plasma spray technique as catalyst for have been reported, where the reagents were firstly vaporized and then recombined to Fe_3C during the cooling phase.[48] Thus the possibility of Cu adsorption on metal surfaces depends on the preparation methods and procedures in the corresponding experiments. The adsorption energies with respect to the bulk fcc-Cu energy were given for comparison.

2.2. Models: All Cu_n clusters in gas phase were calculated using a 15Å×15Å×15Å cubic unit cell at the Γ point. By using a 10×10×10 *k*-point grid, the computed equilibrium lattice constant and magnetic moment of bulk body-centered cubic (bcc) Fe are 2.83 Å and 2.22 μ_B, respectively, which agree well with the experimental values of 2.86 Å and 2.22 μ_B.[49,50] Apart from the most stable Fe(110) surface in our previous work,[39] the less stable Fe(100) and least stable Fe (111) surfaces as basic structures are considered on the basis of early study about surface energies.[51-53] In order to choose a reasonable periodic slab model, tests were performed to reveal the effects of slab thickness, relaxation thickness on Cu adsorption energy. These results are listed in the Supplementary Information (Table S1).

The Fe_3C phase has an orthorhombic structure with sixteen atoms per unit cell, where eight iron atoms are in the *general* positions (Fe_g), four iron atoms are in the *special* positions (Fe_s) and four carbon atoms are in the interstices. Both Fe_g and Fe_s atoms are fourteen-coordinated but with three and two Fe-C bonds, respectively.[54] The calculated cell parameters (*a* = 5.02 Å, *b* = 6.73 Å, *c* = 4.47 Å) and magnetic moment (Fe_g = 1.88 μ_B, and Fe_s = 1.97 μ_B) agree reasonably with the available experimental data (*a* = 5.09 Å, *b* = 6.74 Å, *c* = 4.52 Å, and the average magnetic moment of Fe = 1.78 μ_B).[55,56] For the Fe_3C phase, apart from the most stable Fe_3C(001) surface in our previous work,[39] the less stable Fe_3C(010) and the least stable Fe_3C(100) surfaces are considered on the basis of previous studies.[57-60] Both Fe_3C(100) and Fe_3C(001) have exposed surface iron and carbon atoms, while Fe_3C(010) has only exposed surface iron atoms. Model tests were also performed to find a reasonable periodic slab model on the basis Cu adsorption energy and these results are listed in the Supplementary Information (Table S2). To model Fe_3C(100), the slab consisting of eight Fe layers and four C layers (8Fe+4C) with a slab thickness of 4.66 Å is used, where the top four Fe layers and two C layers (4Fe+2C) are allowed to relax, and the other bottom layers are fixed in their bulk positions. For Fe_3C(010), the slab consisting of six Fe layers and two C layers (6Fe+2C) with a slab thickness of 5.81 Å is used, and the top three Fe layers and one C layers (3Fe+1C) are allowed to relax, while the other bottom layers are fixed in their bulk positions.

To model Fe(100), the *p*(4×4) slab consisting of four-layer iron are used, where the top two layers are relaxed and the bottom two layers are fixed in their bulk positions. For Fe(111), a *p*(3×3) super cell with six-atomic-layer is used, where the top four layers are relaxed and the bottom two layers are fixed. According to the lattice sizes, 3×3×1 k-point grid sampling within the Brillouin zones was set for Fe(100), while 2×2×1 for Fe(111). For studying Cu_n adsorption on the Fe_3C(010) and Fe_3C(100) surfaces, a *p*(2×2) unit cell is used to ensure enough surface area for Cu_n cluster adsorption. According to the lattice sizes, 3×3×1 k-point grid sampling within the Brillouin zones was set. All slab models have a 15 Å vacuum region to exclude significant interaction between the slabs for Fe and Fe_3C surfaces.

3. Results

3.1. Cu_n on Fe(100): For Cu_n adsorption on this surfaces, both aggregation and dispersion are computed. For aggregation mode, the clusters of Cu_n (*n* = 4−7) which are more stable in gas phase and have been adopted in the previous study[39] also are considered. Despite different initial structures in gas phase of these clusters, they become the same adsorption configuration after optimization in some cases, and only those stable configurations have been compared and discussed. The same clusters are also considered on the Fe(111) surface. As shown in Fig. 1, the Fe(100) surface has top (**T**), bridge (**B**), and hollow (**H**) adsorption sites. The results for Cu_n (*n* = 1-7, 13) adsorption are listed in Table 1 and the adsorption configurations are shown in Fig. 2. The detailed adsorption structures and energies after optimization are given in the Supplementary Information (Fig. S1-4).

(a) Cu_n adsorption: The most stable adsorption site for one Cu atom is the **H** site having the coordination number of five to the

exposed surface iron atoms; and the adsorption energy is -3.16 eV. For Cu_2, both two Cu atoms are located at the neighboring **H** sites with the Cu-Cu distance of 2.48 Å, which is longer than that in gas phase (2.22 Å). The computed adsorption energy is -6.85 eV, which is larger than twice of single Cu atom adsorption (-6.32 eV), indicating additional Cu-Cu interaction.

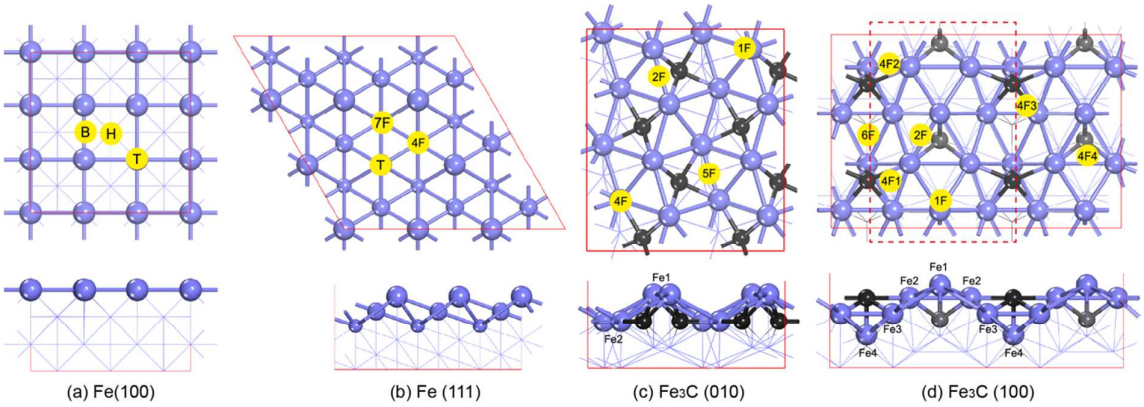

Fig. 1 Possible adsorption sites on the Fe (100), Fe (111), Fe_3C(010) and Fe_3C(100) surfaces; top (**T**), bridge (**B**), hollow (**H**), one-fold (**1F**), two-fold (**2F**), four-fold (**4F, 4F1**, **4F2, 4F3** and **4F4**), five-fold (**5F**), six-fold (**6F**) and seven-fold (**7F**) sites (blue balls for Fe atoms, dark balls for the first layer C atoms; grey balls for the second layer C atoms)

Table 1 Adsorption energies [$E(Cu_{n/ads})$; eV], average adsorption energies [$E(Cu_{ads/av})$; eV], stepwise adsorption energies [$\Delta E(Cu_{ads})$; eV], average aggregation energies [$E_{agg}(Cu_{ads})$; eV], stepwise growth energies [$E_{growth}(Cu_{ads})$; eV], coordination numbers (CN) with surface Fe atoms, average Cu–Cu distances ($d_{Cu\text{-}Cu}$, Å), and average Bader charges (q, e) for Cu_n (n = 1–7, 13) on Fe(100)

Cu_n	$E(Cu_{n/ads})$[a]	$E(Cu_{ads/av})$	$\Delta E(Cu_{ads})$	$E_{agg}(Cu_{ads})$[b]	$E_{growth}(Cu_{ads})$[c]	CN	$d_{Cu\text{-}Cu}$[d]	q
Fe(100)-Cu_1	-3.16 (0.35)	-3.16	-3.16	0.00	0.00	5		-0.28
Fe(100)-Cu_2-a/b	-6.85 (0.16)	-3.42	-3.69	-0.27 (-1.13)	-0.53 (-2.26)	10	2.48 (2.22)[c]	-0.27
Linear-based growth mode								
Fe(100)-Cu_3-a	-10.38 (0.13)	-3.46	-3.53	-0.30	-0.37	15	2.56	-0.25
Fe(100)-Cu_4-a	-13.99 (0.02)	-3.50	-3.61	-0.34	-0.45	20	2.83	-0.22
Fe(100)-Cu_5-a	-17.56 (-0.05)	-3.51	-3.57	-0.35	-0.42	24	2.79	-0.21
Fe(100)-Cu_6-a	-21.32 (-0.30)	-3.55	-3.76	-0.40	-0.60	30	2.75	-0.20
Square-based growth mode								
Fe(100)-Cu_3-b	-10.38 (0.13)	-3.46	-3.53	-0.30 (-1.23)	-0.37 (-1.43)	14	2.53 (2.35)	-0.24
Fe(100)-Cu_4-b	-14.07 (-0.06)	-3.52	-3.69	-0.36 (-1.59)	-0.53 (-2.67)	20	2.63 (2.36)	-0.21
Fe(100)-Cu_5-b	-17.61 (-0.10)	-3.52	-3.55	-0.36 (-1.72)	-0.39 (-2.26)	24	2.63 (2.36)	-0.21
Fe(100)-Cu_6-b	-21.32 (-0.30)	-3.55	-3.70	-0.39 (-1.92)	-0.55 (-2.88)	28	2.67 (2.36)	-0.20
Fe(100)-Cu_7-a/b	-25.05 (-0.53)	-3.58	-3.73	-0.42 (-2.04)	-0.57 (-2.80)	33	2.73 (2.42)	-0.19
3D structures								
Fe(100)-Cu_5-c	-17.09 (0.43)	-3.42	-3.02	-0.26	0.14	21	2.61	-0.18
Fe(100)-Cu_6-c	-20.63 (0.39)	-3.44	-3.01	-0.28	0.14	26	2.62	-0.19
Fe(100)-Cu_7-c	-24.48 (0.04)	-3.50	-3.16	-0.34	0.00	31	2.59	-0.18
Cu_{13}								
Fe(100)-Cu_{13}-a	-47.31 (-1.78)	-3.64		-0.48		55	2.79	-0.15
Fe(100)-Cu_{13}-c1	-46.60 (-1.06)	-3.58		-0.43		48	2.74	-0.15
Fe(100)-Cu_{13}-c2	-45.30 (0.23)	-3.48		-0.33		37	2.61	-0.14

(a) The values in parenthesis are obtained with respect to the bulk Cu energy. (b-d) The values in parenthesis are that of Cu_n clusters in gas phase (from Ref 39)

Adding one Cu atom to Cu_2 gives two most stable adsorption configurations of Cu_3 with the same adsorption energies (-10.38 eV), the linear **Cu_3-a** as well as the branched **Cu_3-b**. For Cu_4 adsorption, there are two adsorption configurations in close adsorption energies, i.e., the linear **Cu_4-a** (-13.99 eV) and the square **Cu_4-b** (-14.07 eV). For Cu_5 adsorption, the linear-based **Cu_5-a** as well as the square-based **Cu_5-b** also have close adsorption energies (-17.56 and -17.61 eV, respectively). The same is also found for Cu_6 adsorption, and they have the same adsorption energies (-21.23 eV) despite their large structural differences. From both growth modes, we finally obtained the most stable adsorption configuration for Cu_7 with adsorption energy of -25.05 eV.

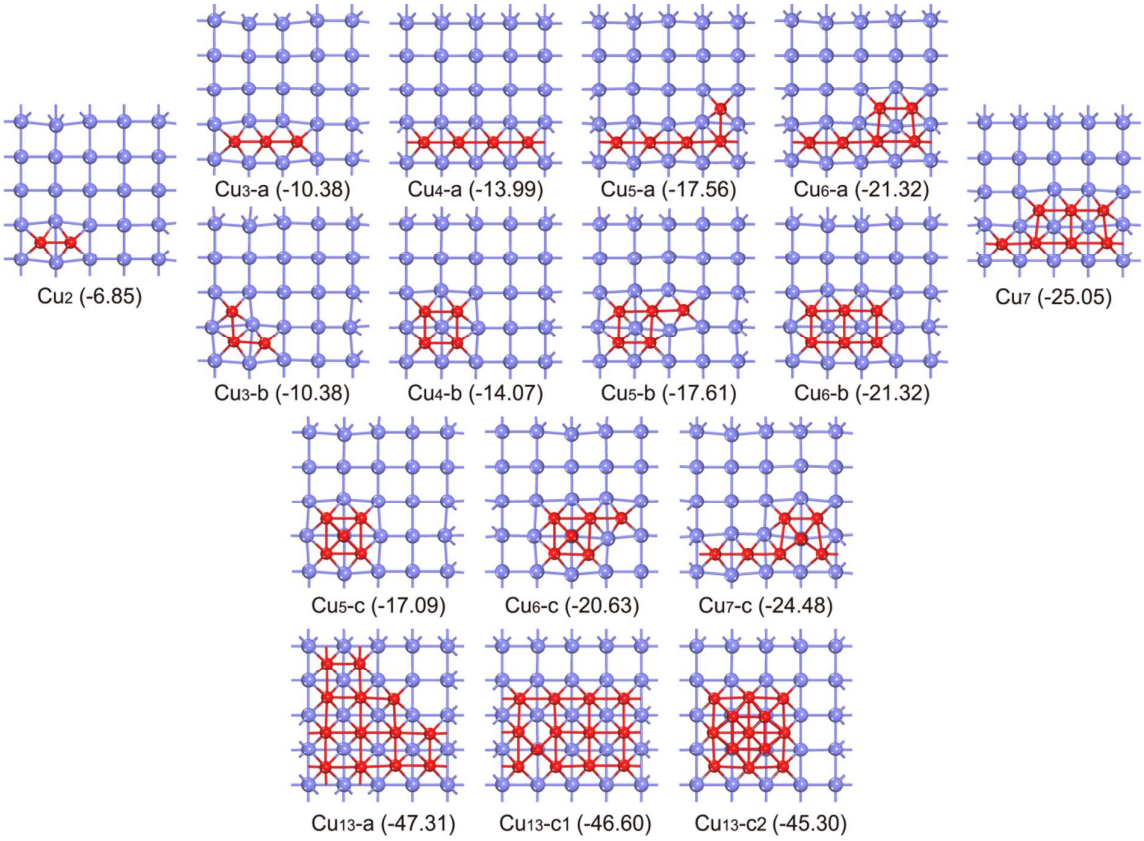

Fig. 2 Structures for Cu_n (n = 1–7, 13) on the Fe(100) surface (blue ball for Fe atoms; and red ball for Cu atoms)

For n = 4-6, the Cu_4 chain of linear-based growth mode is not an isolated cluster, but rather interacts with the neighboring units to form a row of Cu atoms due to periodicity. However, both growth modes have very close adsorption energies and this is due to their equal numbers of Fe-Cu as well as Cu-Cu bonding. This is again confirmed by the adsorbed Cu_7 structure. For searching the surface size effect, we computed Cu_4 and Cu_5 adsorption modes using the larger p(5×4) slab size (Supplementary Information Fig. S25). For Cu_4, three are three adsorption modes, the isolated square one and the linear one interacting with the neighboring units (along the short edge) as well as the isolated linear one (along the long edge). The former two modes which have the same Cu-Cu bonding and close adsorption energies (-14.06 and -14.07 eV) are more stable than the third one (-13.96 eV) which has one Cu-Cu bonding less. For Cu_5, four adsorption modes are computed; the square-based one, the linear one interacting with the neighboring units (along the long edge) and the L-form one interacting with the neighboring units (along the short edge) as well as the isolated L-form one (along the long edge). The former three modes having the same number of Cu-Cu bonding are close in adsorption energies (-17.60, -17.55, -17.57 eV), and they are more stable than the last one (-17.48 eV) which has one Cu-Cu bonding less. On large enough surface size, it is to expect that square based modes should be more favorable energetically, and therefore monolayer adsorption configurations with more squares are favored with the increase of coverage.

To confirm this proposal, the most stable 3D configurations for *n* = 5-7 in our study are also listed in Fig. 2. All these clusters have one Cu atom over the square. The adsorption energy of the most stable 3D Cu_5 (**Cu_5-c**, -17.09 eV), Cu_6 (**Cu_6-c**, -20.63 eV) and Cu_7 (**Cu_7-c**, -24.48 eV) isomers is 0.52, 0.69 and 0.57 eV lower than that of the most stable 2D isomers, respectively. Compared to their 2D isomers, these 3D isomers have more Cu-Cu bonding, but less Fe-Cu bonding, revealing stronger Fe-Cu bonding over Cu-Cu bonding on surface.

To further confirm this result, we used the large Cu_{13} models, where the 2D model has a monolayer structure (**Cu_{13}-a**) and one 3D model (**Cu_{13}-c1**) has a Cu_{12} monolayer covered by a Cu atom over a square surface. The second 3D model (**Cu_{13}-c2**) has a bilayer structure, where the first layer has a Cu_9 monolayer and the second layer has one Cu_4 square unit. The monolayer 2D structure (**Cu_{13}-a**; -47.31 eV) is more stable than the two 3D structures (**Cu_{13}-c1**; -46.60 eV and **Cu_{13}-c2**; -45.30 eV), suggesting a layer-by-layer mode for further Cu growth, as supported by the previous low-energy electron diffraction and reflection high-energy electron diffraction studies,[61-63] i.e.; Cu over-layers grow layer-by-layer on the Fe(100) surface, and maintain the bcc phase as the iron substrate. In addition, the computed single-point energies for **Cu_{13}-a** and **Cu_{13}-c2** on Fe(100) in gas phase show that the 3D cluster is 7.25 eV more stable than the planar 2D structure, indicating stronger Fe-Cu bonding on surface than Cu-Cu bonding in gas phase. The same trend is also shown by the much lower average aggregation energies (negative of the binding energies) of Cu_n on surface than in gas phase (Table 1). Therefore, one can expect that Cu prefers monolayer structures on Fe(100), while 3D clusters in gas phase. It is noted that none of our Cu_{13} models represents the most stable gas phase structure,[64] and the adsorption of this most stable gas phase cluster on Fe(100) would be very unstable due to the much lower number for Fe-Cu bonding.

(b) Cu_n mobility: To understand the mobility of the adsorbed Cu atoms on Fe(100), the migration barrier of the adsorbed single Cu atom on the surface from one **H** site to another **H** site has been computed. In the transition state (Fig. 3), the Cu atom is located at the bridge (**B**) site; and the barrier is 0.52 eV, which agrees well with the previous result (0.50 eV).[39] The diffusion of the adsorbed single Cu atom from H site to T site is not considered due to the highly endothermic process (1.03 eV).

In addition, two isomerization pathways of **Cu_4**-b are considered. One is the square-diamond-square transition to **Cu_4-c**, the computed barrier is 1.10 eV and the process could be used to estimate surface translation; the other one is the distortion to **Cu_4-d,** the computed barrier is 0.87 eV and the process could be used to estimate stepwise isomerization of surface Cu_n (Fig. 3). Similar to that on Fe(110), the diffusion of an edge Cu atom is easier than the translation of multi-Cu atoms. Nevertheless, compared with Cu_n on Fe(110) (0.42/0.28 eV),[39] the adsorbed Cu_n structures on Fe(100) have lower mobility.

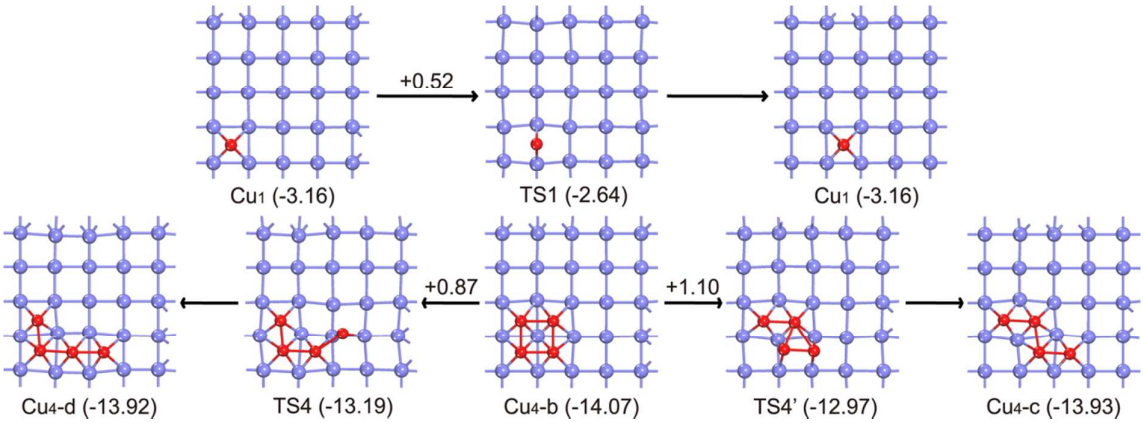

Fig. 3 The transition states for the degenerated Cu_1 migration (TS1) and Cu_4 isomerization (TS4) on the Fe(100) surface (blue ball for Fe atoms; and red ball for Cu atoms)

3.2 Cu_n on Fe(111)

(a) Cu_n adsorption: Because of its more open surface structure, Cu_n adsorption on Fe(111) is very different from those on

Fe(110) and Fe(100). As shown in Fig. 1b, for single Cu atom, only the adsorption at **7F**, **4F** and **T** sites is located. The **7F** site has three first layer Fe atoms, three second layer Fe atoms and one third layer Fe atom; the **4F** site has one second layer Fe atom and three first layer Fe atoms; and the **T** site is atop of the first layer Fe atoms. The most stable adsorption configuration on the surface is located at the **7F** site.

There are also two growth modes; the dispersion one (**Cu_n-a**) without forming direct Cu-Cu bonding and the aggregation one (**Cu_n-b**) with direct Cu-Cu bonding. These results are listed in Table 2 and the adsorption configurations are shown in Fig. 4. For the dispersion mode **Cu_n-a** (n = 2-7), all Cu atoms are located vertically on the top of the third layer Fe atoms without direct Cu-Cu bonding (**7F** site). All these adsorption configurations have nearly the same adsorption energies and stepwise adsorption energies, revealing that all the adsorbed Cu atoms on the surface are independent, and they do not interact with each other.

For the aggregation mode **Cu_n-b**, the surface Cu atoms adsorb at either the **7F** site or the nearest **4F** site (the second stable adsorption site) to form Cu_n clusters. The **Cu_2-b** structure has one Cu atom at the **7F** site and another Cu atom at the nearest **4F** site. In the **Cu_3-b** structure, two Cu atoms adsorb at the **7F** sites and one Cu atom adsorbs at the nearest **4F** site. The **Cu_4-b** structure is star-like, where three Cu atoms at the **7F** sites and one Cu atom at the nearest **4F** site. For the **Cu_5-b** structure in U-shape, three Cu atoms adsorb at the **7F** site while the other two Cu atoms adsorb at the nearest **4F** site. Both **Cu_6-b** and **Cu_7-b** are formed on the basis of **Cu_5-b** by adding a **7F**-Cu atom to the side of the original **4F**-Cu atoms, namely forming successive star-like structures.

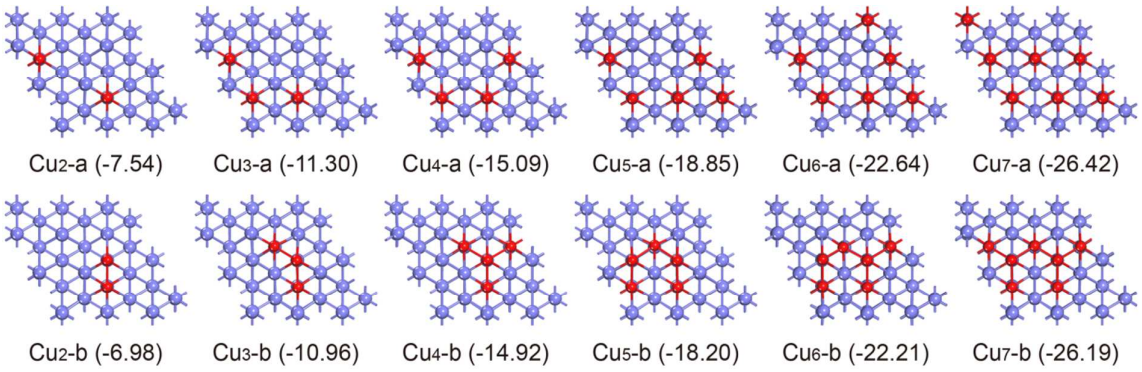

Fig. 4 Structures for Cu_n (n = 2–7) on the Fe(111) surface (blue balls for Fe atoms; and red balls for Cu atoms)

Table 2 Adsorption energies [$E(Cu_{n/ads})$; eV],[a] average adsorption energies [$E(Cu_{ads/av})$; eV], stepwise adsorption energies [$\Delta E(Cu_{ads})$; eV], average aggregation energies [$E_{agg}(Cu_{ads})$; eV], stepwise growth energies [$E_{growth}(Cu_{ads})$; eV], coordination numbers (CN) with surface Fe atoms, average Cu–Cu distances (d, Å), and average Bader charges (q, e) for Cu_n (n = 1–7, 13) on Fe(111)

Cu_n	$E(Cu_{n/ads})$[a]	$E(Cu_{ads/av})$	$\Delta E(Cu_{ads})$	$E_{agg}(Cu_{ads})$	$E_{growth}(Cu_{ads})$	CN	d	q
Fe(111)-Cu_1	-3.77 (-0.27)	-3.77	-3.77	0.00	0.00	7	-	-0.27
Dispersed growth mode								
Fe(111)-Cu_2-a	-7.54 (-0.53)	-3.77	-3.76	0.00	0.01	14	-	-0.26
Fe(111)-Cu_3-a	-11.30 (-0.79)	-3.77	-3.77	0.00	0.00	21	-	-0.25
Fe(111)-Cu_4-a	-15.09 (-1.08)	-3.77	-3.79	0.00	-0.02	28	-	-0.24
Fe(111)-Cu_5-a	-18.85 (-1.33)	-3.77	-3.76	0.00	0.02	35	-	-0.22
Fe(111)-Cu_6-a	-22.64 (-1.63)	-3.77	-3.80	0.00	-0.02	42	-	-0.21
Fe(111)-Cu_7-a	-26.42 (-1.90)	-3.77	-3.77	0.00	0.00	49	-	-0.19
Star-like growth mode								
Fe(111)-Cu_2-b	-6.98 (0.03)	-3.49	-3.20	0.28	0.57	11	2.48	-0.22
Fe(111)-Cu_3-b	-10.96 (-0.45)	-3.65	-3.98	0.12	-0.21	18	2.49	-0.23
Fe(111)-Cu_4-b	-14.92 (-0.91)	-3.73	-3.96	0.04	-0.19	25	2.53	-0.22

Fe(111)-Cu_5-b	-18.20 (-0.68)	-3.64	-3.28	0.13	0.49	29	2.49	-0.21
Fe(111)-Cu_6-b	-22.21 (-1.19)	-3.70	-4.01	0.07	-0.24	36	2.51	-0.20
Fe(111)-Cu_7-b	-26.19 (-1.67)	-3.74	-3.98	0.03	-0.21	43	2.51	-0.20

(a) The values in parenthesis are obtained with respect to the bulk Cu energy.

On the basis of the computed adsorption energies, it is clearly to see that the dispersion mode is more stable than aggregation mode with direct Cu-Cu binding by 0.56, 0.35, 0.17, 0.65, 0.43, 0.23 eV for n = 2-7, respectively. Furthermore the average aggregation energies of Cu_n on Fe(111) are zero for dispersion mode and positive for aggregation mode, indicating that the dispersion mode is energetically more preferred at low coverage. Since the energy differences between **Cu_4-a** and **Cu_4-b** as well as **Cu_7-a** and **Cu_7-b** are very small, and both **Cu_4-b** and **Cu_7-b** configurations are star-like, it is to expect that further coverage increase will result in the formation of adsorption configurations having star-like (Cu_4) structural unit. Indeed, the dispersed growth mode is a perfect epitaxial Cu growth on Fe(111), and the formation of star-like units at high coverage should follow the layer-by-layer growth mode.

(b) Cu_n mobility: For the migration of the single adsorbed Cu atom from one **7F** site to another **7F** site, the computed barrier is 0.79 eV. In the transition state (Fig. 5), the Cu atom is located at the qusi-**4F** site. The diffusion of the single adsorbed Cu atom from the most stable **7F** site to the least stable **T** site is unlikely because of their larger energy difference (1.96 eV).

In addition, we also computed the transition from the two dispersed Cu atoms in **2Cu** to the two aggregated Cu atoms in **Cu_2-b**. The computed barrier is 0.63 eV (0.07 eV for the back reaction), and the reaction is endothermic by 0.56 eV. Therefore, the dispersion process is favored not only thermodynamically but also kinetically.

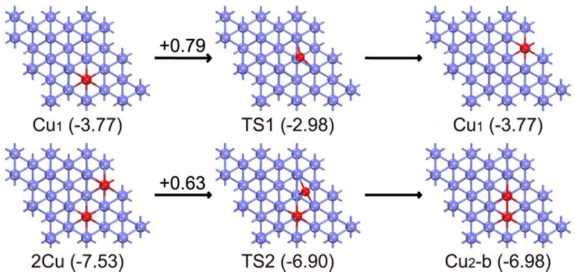

Fig. 5 Transition states for the degenerated Cu_1 migration (TS1) and the aggregation from 2Cu to Cu2-b (TS2) (blue ball for Fe atoms; and red ball for Cu atoms)

3.3. Cu_n on Fe_3C(010): The Fe_3C(010) surface has only two Fe atom layers exposed, and the iron atoms of both layers are in a zigzag arrangement. As shown in Fig. 1c, four adsorption sites are located, i.e., the five-fold (**5F**), four-fold (**4F**), two-fold (**2F**), and one-fold (**1F**) sites. The **5F** site has three Fe1 and two Fe2 atoms; the **4F** site has three Fe1 atoms and one Fe2 atom; the **2F** site bridges two Fe1 atoms, and the **1F** site is atop one Fe1 atom. The detailed adsorption energies and structure information of Cu_n (n = 1-7, 13) on Fe_3C(010) are listed in Table 3, the adsorption configurations are shown in Fig. 6.

Our results in the Supplementary Information (Tables S3-4) show that the adsorption energies of the adsorbed Cu atoms depend highly on the coordination number (CN) with the exposed surface iron (CN-Fe) and surface carbon (CN-C) atoms, i.e.; the higher the CN, the stronger the adsorption. In addition, the number of Cu-Cu bonding (NB-Cu) also affects the adsorption energies. For Cu_n ($n \geq 4$), three adsorption modes are examined; i.e., the dispersed and aggregated modes, where all Cu atoms interact with the exposed surface atoms, as well as the two-layer 3D cluster mode in which only the first layer Cu atoms interact with the exposed surface atoms. Because of the large numbers of adsorption configurations, we discussed only the most stable dispersed and aggregated as well as the two-layer 3D structures, and the other less stable adsorption structures along with their energies are given in the Supplementary Information (Fig. S9-24).

(a) Cu_n adsorption: The most stable adsorption configuration for one Cu atom is the **5F** site, and the adsorption energy is -3.39 eV. For *n* = 2, the dispersed mode with two Cu atoms separately located at the **5F** sites (**Cu_2-a**) is less stable, while the aggregated mode (**Cu_2-b**) having two **5F**-sited Cu atoms bonded is more stable (-6.79 vs. -6.98 eV). For *n* = 3 and 4, both modes have all Cu atoms adsorbed at the **5F** sites, and the dispersed mode (**Cu_3-a**/**Cu_4-a**; -10.17/-13.55 eV) is less stable than the zigzag linear aggregated mode (**Cu_3-b**/**Cu_4-b**; -10.57/-14.42 eV).

For further growth to Cu_5, the resulted dispersed mode (**Cu_5-a**, -16.61 eV) has the newly added Cu atom adsorbed at the **2F** site and bonded to one **5F**-sited Cu atom to form a Cu_2 unit, while the aggregated mode (**Cu_5-b**, -17.77 eV) has the newly added Cu atom adsorbed at the **5F** site separated with the Cu_4 unit (**Cu_4-b**+**5F**) is more stable. In addition, the two-layered Cu_5 cluster **Cu_5-c** (tetragonal pyramid, -15.97 eV) is less stable than **Cu_5-b** by 1.80 eV.

Table 3 Adsorption energy [$E(Cu_{n/ads})$; eV], average adsorption energy [$E(Cu_{ads/av})$; eV], stepwise adsorption energy [$\Delta E(Cu_{ads})$; eV], average aggregation energy [$E_{agg}(Cu_{ads})$; eV], stepwise growth energy [$E_{growth}(Cu_{ads})$; eV], coordination number (CN) with surface Fe and C atoms, number of Cu–Cu bond (NB-Cu), average Cu–Cu distance (*d*, Å), and average Bader charge (q, e) for Cu_n (*n* = 1–7, 13) on $Fe_3C(010)$

	$E(Cu_{n/ads})$[a]	$E(Cu_{ads/av})$	$\Delta E(Cu_{ads})$	$E_{agg}(Cu_{ads})$	$E_{growth}(Cu_{ads})$	CN-Fe	CN-C	NB-Cu	*d*	Q
Cu1	-3.39 (0.12)	-3.39				5				-0.13
				Dispersed mode						
Cu2-a	-6.79 (0.22)	-3.4			-0.01	10	0	0		-0.11
Cu3-a	-10.17 (0.34)	-3.39			0.01	15	0	0		-0.11
Cu4-a	-13.55 (0.46)	-3.39			0.00	20	0	0		-0.1
Cu5-a	-16.61 (0.90)	-3.32			0.33	22	0	0		-0.09
Cu6-a	-19.75 (1.27)	-3.29			0.25	24	0	0		-0.08
				Aggregated mode						
Cu2-b	-6.98 (0.03)	-3.49	-3.59	-0.10	-0.20	10	0	1	2.54	-0.12
Cu3-b	-10.57 (-0.07)	-3.52	-3.60	-0.14	-0.21	15	0	2	2.54	-0.11
Cu4-b	-14.42 (-0.41)	-3.61	-3.85	-0.22	-0.46	20	0	4	2.58	-0.11
Cu5-b	-17.77 (-0.26)	-3.55	-3.35	-0.17	0.04	25	0	4	2.58	-0.09
Cu6-b	-21.39 (-0.38)	-3.57	-3.62	-0.18	-0.23	27	0	7	2.56	-0.09
				3D structures						
Cu5-c	-15.97 (1.54)	-3.19				14	0	8	2.49	-0.07
Cu6-c	-19.81 (1.21)	-3.30				19	0	10	2.50	-0.07
				Cu_7 and Cu_{13}						
Cu7	-24.96 (-0.44)	-3.57	-3.57	-0.18	-0.18	32	0	8	2.56	-0.08
Cu13-a	-47.50 (-1.97)	-3.65		-0.27		50	0	27	2.57	-0.06
Cu13-b	-46.72 (-1.18)	-3.59				48	0	28	2.56	-0.05
Cu13-c	-44.54 (1.00)	-3.43				38	0	30	2.52	-0.05

(a) The values in parenthesis are obtained with respect to the bulk Cu energy.

On the basis of the three modes of Cu_5, the three corresponding adsorption modes of Cu_6 are computed. In **Cu_6-a** (-19.75 eV), the newly added **2F**-sited Cu atom bridging two **5F**-sited Cu atoms forms a Cu_4 unit while the last two Cu atoms are still dispersed after optimization. In the aggregated **Cu_6-b** (-21.39 eV), the newly added **2F**-sited Cu atom fuses the single **5F**-sited Cu atom and the Cu_4 unit to a branched Cu_6 structure, and **Cu_6-b** is more stable than **Cu_6-a** by 1.64 eV. The two-layer 3D structure (**Cu_6-c**) has a Cu atom substituted tetragonal pyramid, and the adsorption energy is -19.81 eV, lower than that of **Cu_6-b** by 1.58 eV.

Further growth to Cu_7 based on **Cu_6-b** is examined. The structures with all Cu atoms aggregated (-24.96 and -24.83 eV) have very close adsorption energies with the configuration having separately adsorbed Cu_3 and Cu_4 units (-24.89 eV). Only the most

stable (-24.96 eV) configuration is shown in the Fig. 6, while others are given in the Supplementary Information (Fig. S15).

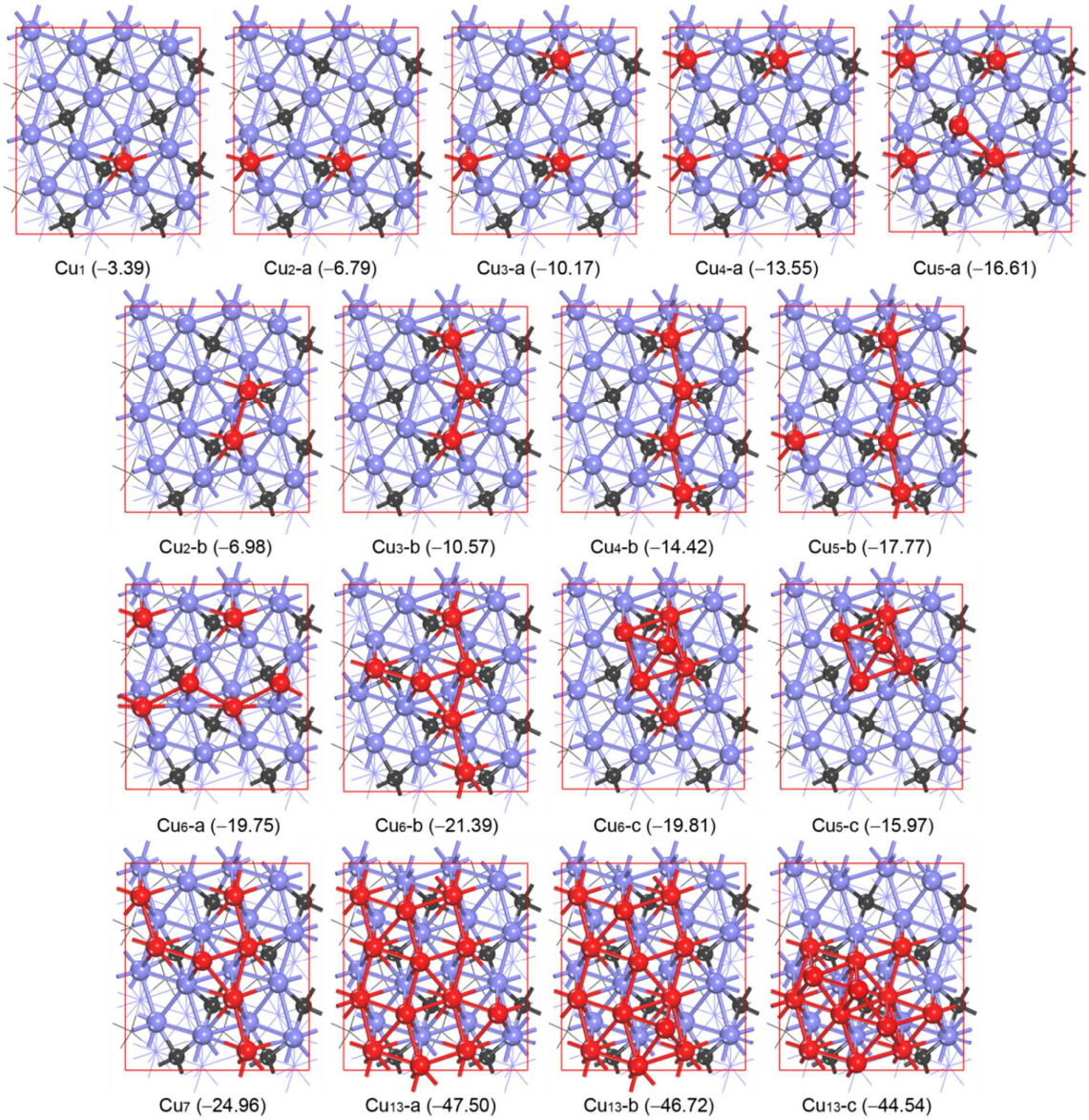

Fig. 6 Most stable adsorption configurations of Cu_n (n = 1–7, 13) on the $Fe_3C(010)$ surface (blue balls for Fe atoms, black balls for C atoms, and red balls for Cu atoms)

The large size Cu_{13} adsorption is examined. The aggregated mode (**Cu_{13}-a**) has a monolayer structure with eight **5F**-sited Cu atoms and five **2F**-sited Cu atoms bonded as a patch, and the adsorption energy is -47.50 eV. The two-layer 3D configurations **Cu_{13}-b** (one second-layered Cu atom, -46.72 eV) and **Cu_{13}-c** (three second-layered Cu atoms, -44.54 eV) are, however, less stable.

The computed results of Cu_n adsorption on the metallic $Fe_3C(010)$ surface show that the aggregated modes are more stable than the dispersed and two-layer 3D modes (n = 2-6); monolayer structure is preferred at high coverage. It is noted that for n = 4-7, each most stable adsorption configuration has a Cu_4 chain interacting with the neighboring units. The most stable Cu_{13} structure has three cross-linked Cu_4 chains. The average adsorption energies of the most stable Cu_n adsorption configurations are larger than that of single Cu atom, indicating that both surface Fe-Cu and Cu-Cu bonding contribute to the adsorption energies. For studying the surface size effect, we computed two Cu_5 adsorption structures using the larger $p(2\times3)$ slab size (Supplementary Information Fig. S26), the one with a Cu_5 chain and the other one having a Cu_4 chain and an isolated Cu atom (Cu_5-b like). The former is more stable than the later (-17.78 and -17.57 eV, respectively). On large enough surface size, it is to expect that chain

modes should be more favorable energetically.

(b) Cu_n mobility: The diffusion of single Cu atom on the $Fe_3C(010)$ surface is relatively simple. There are two pathways, **P1** along the [100] direction and **P2** along the [001] direction (Fig. 7). Since no transition states could be located, the diffusion process can be considered as Cu atom hopping between different adsorption sites. Due to the different adsorption energies at **4F** and **2F** sites, the energy level of **P1** (**5F** → **4F** → **5F**) is lower than that of **P2** (**5F** → **2F** → **4F** → **5F**) (0.21 vs. 0.79 eV). Indeed, **P1** leads to the formation of the zigzag line found in **Cu_4-b**. This further verifies the conclusion of Cu_n growth mode obtained above.

3.4. Cu_n on $Fe_3C(100)$: The schematic structure and adsorption sites of Cu atom on $Fe_3C(100)$ are shown in Fig. 1d. The $Fe_3C(100)$ surface is highly ordered and can be divided into periodically repeated iron regions separated by surface carbon lines. Within one region, there are three iron layers exposed on the surface, including one first-layer Fe atom line (Fe1), two symmetrical second-layer Fe atom lines (Fe2) and two symmetrical third-layer Fe atom lines (Fe3) in the order of Fe3-Fe2-Fe1-Fe2-Fe3, while the Fe3 lines neighbor the boundary C atom lines. The $Fe_3C(100)$ surface has different sites for Cu adsorption, i.e.; the six-fold (**6F**) site is located on the carbon line and consists of five Fe atoms and one C atom; the two-fold (**2F**) site bridges the first and second layer iron atoms; the one-fold (**1F**) site is atop the first layer iron atom. For the four-fold sites, the **4F1, 4F2** and **4F3** sites have one carbon atom and three iron atoms, and the **4F4** site has four Fe atoms.

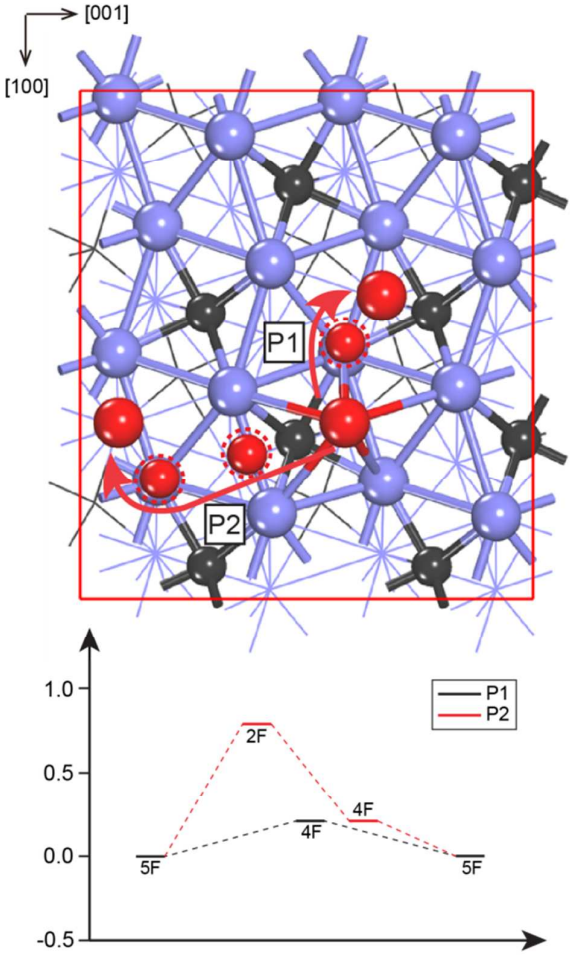

Fig. 7 Diffusion pathways of single Cu atom on the $Fe_3C(010)$ surface (blue balls for Fe atoms, black balls for C atoms, and red balls for Cu atoms)

(a) Cu_n adsorption: These results are listed in Table 4 and the adsorption configurations are shown in Fig. 8. The most stable adsorption site of one Cu atom on $Fe_3C(100)$ is the **6F** site and the adsorption energy is -3.58 eV. For Cu_2 adsorption, the dispers-

ed mode **Cu_2-a** has both two Cu atoms at the **6F** sites, and the adsorption energy is -7.17 eV; while the aggregated mode **Cu_2-b** having one Cu atom at the **6F** site and the second Cu atom at the **4F1** site is less stable (-6.98 eV). On the basis of **Cu_2-a** as well as **Cu_2-b**, one dispersed (**Cu_3-a**) and one aggregated (**Cu_3-b**) most stable adsorption configurations are obtained. Despite remarkable structural differences, they have very close adsorption energies (-10.63 and -10.71 eV, respectively). On the basis of the total coordination numbers (CN-Fe, CN-C and NB-Cu), one general trend can be found, i.e.; the larger the total coordination number, the stronger the adsorption, and configurations having the same coordination numbers are close in adsorption energies.

For *n* = 4, we have located the dispersed (**Cu_4-a**) and aggregated (**Cu_4-b**) as well as the two-layer 3D cluster (**Cu_4-c**, a tetrahedral structure) modes. Both **Cu_4-a** as well as **Cu_4-b** having the same total coordination number (24) are very close in energy (-14.11 and -14.21 eV, respectively), while **Cu_4-c** having lower coordination number (18) is less stable (-12.94 eV).

Since all the most stable **6F** sites have been occupied in **Cu_4-a**, further addition of Cu atoms for the dispersed mode will occupy the **4F4** sites. The resulted adsorption configuration **(Cu_5-a**) has adsorption energy of -17.28 eV. For the aggregated mode (**Cu_5-b**), one additional Cu atom has been added to **Cu_4-b** to form a rhombic ring, and the adsorption energy is -17.71 eV. This energetic difference can be ascribed to their different total coordination numbers (28 vs. 29). For the two-layer 3D cluster model (**Cu_5-c**, a Cu atom substituted tetrahedral structure), the adsorption energy is -16.86 eV, less stable than **Cu_5-b** by 0.86 eV.

Table 4 Adsorption energy [$E(Cu_{n/ads})$; eV], average adsorption energy [$E(Cu_{ads/av})$; eV], stepwise adsorption energy [$\Delta E(Cu_{ads})$; eV], average aggregation energy [$E_{agg}(Cu_{ads})$; eV], stepwise growth energy [$E_{growth}(Cu_{ads})$; eV], coordination number (CN) with surface Fe and C atoms, number of Cu–Cu bond (NB-Cu), average Cu–Cu distance (*d*, Å), and average Bader charge (q, e) for Cu_n (*n* = 1–7, 13) on $Fe_3C(100)$

	$E(Cu_{n/ads})$[a]	$E(Cu_{ads/av})$	$\Delta E(Cu_{ads})$	$E_{agg}(Cu_{ads})$	$E_{growth}(Cu_{ads})$	CN-Fe	CN-C	NB-Cu	*d*	q
Cu1	-3.58 (-0.07)	-3.58				5	1	0		0.16
				Dispersed mode						
Cu2-a	-7.17 (-0.16)	-3.58	-3.59	-0.01	-0.01	10	2	0		0.16
Cu3-a	-10.63 (-0.12)	-3.54			0.12	15	3	0		0.16
Cu4-a	-14.11 (-0.10)	-3.53			0.09	20	4	0		0.16
Cu5-a	-17.28 (0.23)	-3.46			0.40	24	4	0		0.09
Cu6-a	-20.40 (0.61)	-3.40			0.46	28	4	0		0.05
				Aggregated mode						
Cu2-b	-6.98 (0.03)	-3.49			0.17	8	2	1	2.50	0.07
Cu3-b	-10.71 (-0.20)	-3.57	-3.55	0.01	-0.16	13	3	2	2.53	0.09
Cu4-b	-14.21 (-0.20)	-3.55	-3.50	0.02	0.08	16	4	4	2.50	0.05
Cu5-b	-17.71 (-0.20)	-3.54	-3.50	0.03	0.07	18	4	7	2.52	0.03
Cu6-b	-21.20 (-0.18)	-3.53	-3.49	0.04	0.09	20	4	10	2.54	0.02
				3D structures						
Cu4-c	-12.94 (1.07)	-3.23				10	2	6	2.50	0.03
Cu5-c	-16.86 (0.66)	-3.37				16	4	8	2.54	0.05
Cu6-c	-20.33 (0.68)	-3.39				18	4	10	2.53	0.03
				Cu_7 and Cu_{13}						
Cu7	-24.62 (-0.10)	-3.52	-3.42	0.06	0.15	25	5	10	2.54	0.04
Cu13-a	-46.54 (-1.01)	-3.58		0.00		41	8	28	2.55	0.02
Cu13-b	-45.17 (0.37)	-3.47				36	6	29	2.57	0.00
Cu13-c	-45.13 (0.41)	-3.47				42	8	22	2.53	0.01
Cu13-d	-43.30 (2.24)	-3.33				35	6	26	2.52	0.02

(a) The values in parenthesis are obtained with respect to the bulk Cu energy.

For *n* = 6, as expected, the aggregated mode **Cu_6-b** (spiro-connected rhombic ring) is more stable than the dispersed mode **Cu_6-a** (-21.20 vs. -20.40 eV), while **Cu_6-c** (a Cu_2 substituted tetrahedral structure) is least stable (-20.33 eV). Since the aggregated mode becomes more stable than the dispersed mode for n ≥ 3, we further considered only the aggregated model for *n* = 7. All five adsorption configurations have very close adsorption energies (-24.38 to -24.62 eV, Supplementary Information), despite the fact that the most stable one has one separated Cu_6 unit and one isolated Cu atom. This indicates that the aggregation will take place along the iron region at first and then spread over the surface in monolayer structure.

To confirm this proposal, the adsorption structures and energies of several Cu_{13} models are computed. As shown in Fig. 8, the most stable adsorption configuration has a symmetrical Cu_{13} structure along the iron region, and this structure can be considered as two Cu_6 units linked by one **1F**-sited Cu atom in the middle (**Cu_{13}-a**, -46.54 eV). The second one (**Cu_{13}-b**, -45.17 eV), which has the Cu_{13} unit across the carbon line is less stable by 1.37 eV. The third one (**Cu_{13}-c**, -45.13 eV), in which the two Cu_6 units are located in two iron regions and linked by one **2F**-sited Cu atom, is less stable by 1.41 eV. The two-layer 3D cluster adsorption mode (**Cu_{13}-d**, -43.30 eV), in which the first-layer has 11 adsorbed Cu atom on the iron region and two Cu atoms over the first layer, is much less stable. All these confirm the proposed growth mode at high coverage, firstly growing to spiro-connected rhombic Cu_6 units on the edges of one iron region and then linked by **1F**-sited Cu atoms in the middle of the iron region. Similar to that on the $Fe_3C(010)$ surface, for *n* = 4-7 and 13, the most stable adsorption configurations have Cu_4 chains interacting with the neighboring units. On the basis of the results, it can be seen that Cu atoms prefer to disperse at very low coverage (n = 1, 2), and aggregate as belts within the iron region at high coverage (n ≥ 3).

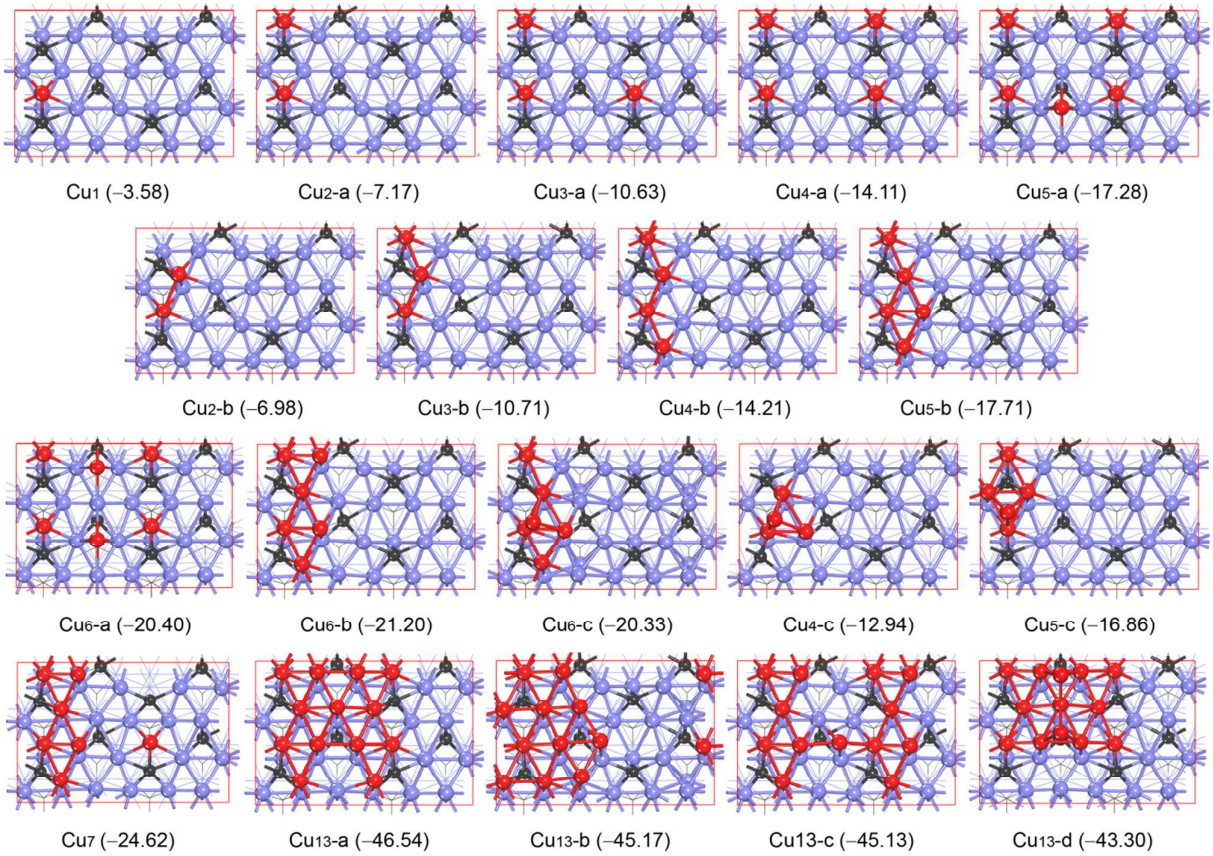

Fig. 8 Most stable adsorption configurations of Cu_n (*n* = 1–7, 13) on the $Fe_3C(100)$ surface (blue balls for Fe atoms, black balls for C atoms, and red balls for Cu atoms)

(b) Cu_n mobility: To understand the stable state of Cu_n on $Fe_3C(100)$, we computed the barriers for single Cu atom diffusion among the most stable adsorption sites (**6F**). As shown in Fig. 9 (top), there are two directions for single Cu atom diffusion, i.e.;

either the [001] or [010] direction. Similar to that $Fe_3C(010)$ surface, Cu diffusion can also be considered as Cu atom hopping between different adsorption sites. As shown in Fig. 9 (bottom), the Cu atom diffusion following the first path (**P1**, **6F** → **2F** → **4F4** → **2F** → **6F**) along the [001] direction from one carbon line crossing the second-layer and first-layer iron atom lines has energy difference of 1.03 eV. In the second path (**P2**, **6F** → **4F3** → **4F1** → **4F2** → **6F**), the Cu atom diffusion along the carbon line in the [010] direction has energy difference of 0.49 eV, which is much smaller than that of **P1**. This is indeed understandable, since the **4F3** site has stronger adsorption energy for single Cu atom than the **2F** site (-3.09 vs. -2.54 eV, Supplementary Information). On $Fe_3C(100)$, the Cu atom can diffuse easily along the [010] direction. This also verifies our above proposed Cu aggregation mechanism, i.e.; Cu aggregation will take place along the iron region at first and then spread over the surface in monolayer structure.

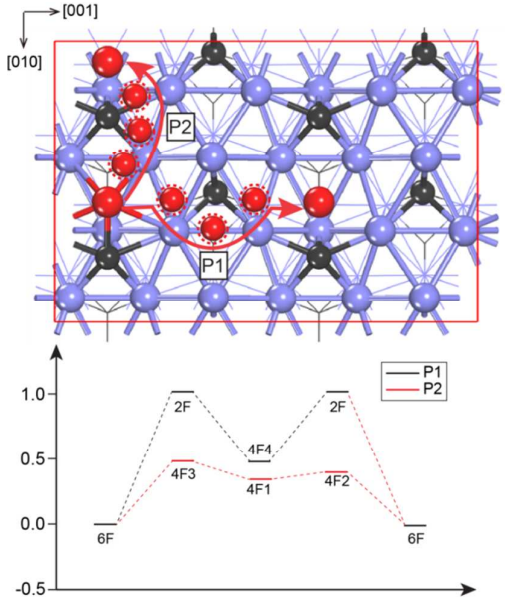

Fig. 9 Diffusion pathways of single Cu atom on the $Fe_3C(100)$ surface

3.5. Discussion

Along with our previous study about the adsorption structures and energies of Cu_n on the most stable Fe(110) and $Fe_3C(001)$ surfaces,[39] we are able to compare the adsorption properties of Cu_n on the less and least stable iron as well as on iron carbide surfaces for understanding the initial stages of copper promotion in Fe-based FTS.

On the most stable Fe(110) and the less stable Fe(100) surfaces, the most stable adsorption configurations favor two-dimensional aggregation instead of surface dispersion and three-dimensional aggregation; and monolayer Cu covered Fe(110) and Fe(100) surfaces can be expected at high coverage. This result is further verified by comparing the two-dimensional monolayer structure and the three-dimensional two-layer structures of Cu_{13}. This spread monolayer preference agrees well with the experimental observation that the reduced Cu species spreads to the metallic Fe surface when treated at 275°C.[28] On the least stable Fe(111) surface, however, the adsorbed Cu atoms favor dispersion instead of aggregation at low coverage, while both dispersion and aggregation modes are possible at high coverage. The driving force for these stable adsorption configurations is the stronger Fe-Cu bonding on the surface than the Cu-Cu interaction in gas phase.

Generally the calculated results reveal that Cu tends to adopt the body-centered cubic lattice structure of the iron substrate in the early stages of deposition (growth) and forms a two-dimensional monolayer at low coverage. Therefore, the formation of metastable body-centered cubic Cu structures on the Fe substrate following the layer-by-layer growth mode can be expected at high coverage, and this epitaxial growth mode of Cu on Fe(001) has been indeed verified by experimental studies.[61-63] Such growth mode has been observed for Fe deposition on the body-centered cubic Mo(111) surface.[65]

The stepwise adsorption energies on the Fe(110) and Fe(100) surfaces indicate that not only the Fe-Cu bonding but also the Cu-Cu bonding determine the adsorption strength and it is therefore possible to get stable Cu adsorption up to monolayer. On the basis of the computed aggregation energies and stepwise growth energies, the adsorbed Cu atoms have higher aggregation ability on the less stable Fe(100) surface than on the most stable Fe(110) surface. On Fe(111), the stepwise adsorption energies are almost constant for Cu_{1-7} as well as the computed aggregation energies and stepwise growth energies are close to zero. All these indicate Cu dispersion instead of aggregation.

On the basis of the average adsorption energies, the adsorption strength of Cu_n (n = 2-7) on the surface, Fe(111) > Fe(100) > Fe(110), correlates with the Cu_n coordination number with the surface Fe atoms (CN-Fe) or the total coordination number (CN, sum of CN-Fe and NB-Cu) as well as with the reverse order of surface stability of Fe(110) > Fe(100) > Fe(111).[51,52] It is found that the adsorbed single Cu atom is mobile and has the increasing diffusion barrier of Fe(110) < Fe(100) < Fe(111). With respect to Cu bulk phase, the Cu_n adsorption energy is positive for n=1-3 and negative for n ≥ 4 on Fe(100) (Table 1) as well as positive for n=1-6 and negative for n ≥ 7 on Fe(110) (Table S5), while negative for n ≥ 1 on Fe(111) (Table 2).

On the most stable $Fe_3C(001)$ and the least stable $Fe_3C(100)$ surfaces[57] the adsorbed Cu atoms prefer to disperse separately at very low coverage and aggregate within the iron region at high coverage. One can expect that the surface Cu atoms will prefer the iron regions of the $Fe_3C(001)$ and $Fe_3C(100)$ surfaces within an appropriate range of Cu coverage. In contrast, only aggregated structures are favored on the less stable metallic $Fe_3C(010)$ surface from low to high coverage, as also found on the most stable Fe(110) and the less stable Fe(100) surfaces. On these carbide surfaces, the more spread aggregation configurations are energetically more favored than two-layer 3D configurations due to the stronger surface Fe-Cu bonding over the Cu-Cu bonding; therefore we can infer that the initial growth of Cu atom on Fe_3C is the layer-by-layer mode. The rather negative stepwise adsorption energies on these carbide surfaces indicate that it is possible to get stable Cu adsorption up to monolayer.

On the basis of the computed average aggregation and stepwise growth energies, the adsorbed Cu atoms have the highest aggregation ability on the less stable metallic $Fe_3C(010)$ surface, revealing the thermodynamically preferred formation of aggregated Cu_n structures. Comparing the average adsorption energies of Cu_n on these carbide surfaces shows that the strongest adsorption is found on the least stable $Fe_3C(100)$ surface for n = 1-3 and on the less stable $Fe_3C(010)$ surface for ≥ 4, while the most stable $Fe_3C(001)$ surface has the weakest adsorption. Taking Cu bulk phase as reference, the Cu_n adsorption energy is positive for n=1-2 and negative for n ≥ 3 on $Fe_3C(010)$ (Table 3) as well as positive for n ≥ 1 on Fe_3C (001) (Table S5); in contrast they are negative for n ≥ 1 on $Fe_3C(100)$ (Table 4).

It is very interesting to compare their adsorption properties between metallic iron and iron carbide surfaces. Both pure iron and iron carbide surfaces have strong adsorption energies, and the strongest adsorption energies are found on Fe(111). Apart from Fe(111), it is found that Cu aggregation properties agree well with the previous experiment studies that Cu agglomerates on reduced catalyst surface (iron surface and carburized iron surface).[27,28] The possible explanation for the discrepancy of Fe(111) is the surface stability and carburization process. More specifically, under typical FTS conditions, it is very difficult or impossible for a direct comparison among different surfaces. Since Fe(111) is least stable and also least exposed. Carburization is a complex process, involving C deposition on the surface, carbon diffusion into surfaces, carbon bulk diffusion and internal carbide formation. During FTS and metallurgy processes, carburization of α-Fe to Fe_3C is prevailing, and the carburization process differs from surface to surface. For example, Fe(110) and Fe(100) have higher carbon diffusion barriers (1.47 and 1.18 (1.35) eV)[66,67] than Fe(111) (0.77 eV),[68] which is also lower than the bulk diffusion barrier from computation (0.86 eV)[69] or experiment (0.87 eV).[70] This result also indicates the easy carburization of Fe(111) suface. All these results revealed that Fe(111) may not stably exist under typical FTS synthesis condition, and should not be detectable.

The adsorption energies on the most stable Fe(110) surface are stronger than on the most stable $Fe_3C(001)$ surface for n = 1-7, 13; and this is in agreement with the experimental observation that iron carbide surface has lower Cu affinity than metallic Fe

surface.[27] This indicates that the experimentally prepared catalysts should mainly consist of these most stable surfaces. Under H_2 reduction atmosphere, for example, Fe(110) represents almost the whole exposed equilibrium shape and only trace of Fe(310) is found; and the other less stable facets are not exposed and detectable.[52,53] The lower Cu affinity of bulk Fe_3C is also in line with the previous theoretical study based on the formation energies of $(Fe_{0.917}Cu_{0.083})_3C$[71] and the partitioning enthalpy[72] of $Fe_{n-1}Cu$ to $Fe_{3q-1}CuC_q$. It is found that substituting Fe atom by Cu atom can destabilize the Fe_3C phase, and during the competitive Cu dissolving in the body-centered cubic Fe and in Fe_3C phases Cu prefers to partition to the Fe phase.

In contrast to these most stable surfaces, less or least stable surfaces behave quite differently. At low Cu coverage, the less stable $Fe_3C(010)$ and the least stable $Fe_3C(100)$ surfaces have stronger Cu adsorption energies than the most stable Fe(110) and less stable Fe(100) surfaces, indicating that $Fe_3C(010)$ and $Fe_3C(100)$ have higher Cu affinities than Fe(110) and Fe(100). At high Cu coverage, $Fe_3C(010)$ and $Fe_3C(100)$ as well as Fe(110) and Fe(100) have close adsorption energies for Cu_{13}, revealing coverage and surface dependent Cu affinities on the less or least stable Fe_3C surfaces. In order to explore the landscapes of Cu adsorption and also the promotion in Fe-based FTS, it is necessary to prepare such less stable surfaces individually. All of these provide great challenges to modern surface sciences and analytic techniques.

Bader charge analysis shows charge transfer from surface Fe atoms to the adsorbed Cu_n units on pure iron surfaces. This is due to their difference in electronegativity between Fe and Cu (1.80 for Fe; and 1.85 for Cu).[73] Furthermore, charge transfer on the Fe(111) and Fe(100) surfaces are more pronounced than on the Fe(110) surface. Charge transfer from surface iron atoms to the adsorbed Cu atoms is also found on the $Fe_3C(010)$ surface, where only surface iron atoms are exposed. Less pronounced net charge transfer is found on the $Fe_3C(001)$ and $Fe_3C(100)$ surfaces having exposed iron and carbon atoms. Detailed analysis shows that Cu atoms interacting with both surface iron and carbon atoms are positively charged. This difference is also in line with the much stronger electronegativity of carbon atom (2.54), which can attract electrons from both iron and copper atoms. With the size increase of the adsorbed Cu_n units, charge transfer decreases accordingly.

4. Conclusion

The adsorption configurations and energies of Cu_n (n = 1-7, 13) on the Fe(110), Fe(100) and Fe(111) surfaces as well as on the $Fe_3C(001)$, $Fe_3C(100)$ and $Fe_3C(010)$ surfaces have been systemically computed by using spin-polarized density functional theory method. Our goal is the understanding into the structures of Cu promoters in Fe-based FTS.

On the Fe(110) and Fe(100) surfaces, the most stable adsorption configurations favor two-dimensional aggregated structures instead of surface dispersion and three-dimensional aggregation at low coverage and the aggregation takes place easily due to the low diffusion barrier as well as the negative average aggregation and stepwise growth energies. Monolayer Cu covered Fe(110) and Fe(100) can be expected at high coverage. It is therefore to expect that the adsorbed Cu atoms almost epitaxially grow on the Fe(110) and Fe(100) surfaces as a layer-by-layer mode at the initial stage, in agreement with the experimental observations. On the Fe(111) surface, the adsorbed Cu atoms favor dispersion rather than aggregation at low coverage, while both dispersion and aggregation modes are possible at high coverage.

The driving force for these stable adsorption configurations is the stronger Fe-Cu binding over the Cu-Cu interaction. Due to the stronger electronegativity of Cu atom over Fe atom, electron transfer from surface Fe atoms to the adsorbed Cu_n has been observed; and more pronounced electron transfer is found on Fe(100) and Fe(111) than on Fe(110).

Compared with the order of surface stability of Fe(110) > Fe(100) > Fe(111), the adsorption strength of single Cu atom has the order of Fe(111) > Fe(110) > Fe(100), while the order of Fe(111) > Fe(100) > Fe(110) for Cu_n (n = 2-7). It is also found that the adsorbed single Cu atom is mobile and has the increasing diffusion barrier of Fe(110) > Fe(100) > Fe(111).

On $Fe_3C(100)$ and $Fe_3C(001)$ with exposed iron and carbon atoms, the adsorbed Cu atoms prefer dispersion at very low coverage and aggregation at high coverage, while aggregation is favored on the $Fe_3C(010)$ surface with only exposed iron atoms. For all

three surfaces, the two-dimensional aggregated configurations are energetically favored than the three-dimensional configurations, therefore we can infer that the initial growth of Cu atom on the Fe_3C surface is a layer-by-layer mode. Furthermore, Cu_n prefer to aggregate firstly as belts in the iron region on $Fe_3C(100)$ and $Fe_3C(001)$ due to the stronger surface Fe-Cu interaction. In an appropriate range of Cu coverage, the surface Cu atoms would be confined to the iron region of the surface.

Compared to the pure iron surfaces, charge transfer between adsorbed Cu atoms and the exposed surface iron and carbon atoms has been observed, while those interacting with the surface carbon atoms are, however, positively charged. On both iron and iron carbide surfaces, the strength of charge transfer decreases with the increase of the Cu_n size.

It should be emphasized that the surfaces considered in this study have different Cu affinities. On the most stable Fe(110) and $Fe_3C(001)$ surfaces, the metallic Fe(110) surface has stronger Cu affinity than the $Fe_3C(001)$ containing exposed surface iron and carbon atoms; and this finding is in agreement with the experimental observations. On the less stable surfaces, however, $Fe_3C(010)$ and $Fe_3C(100)$ surfaces have stronger Cu affinities than the Fe(110) and Fe(100) surfaces at low coverage and close affinities at high coverage, indicating surface and coverage dependent Cu affinities. It is therefore necessary to prepare all these less stable surfaces individually in exploring Cu adsorption and promotion in Fe-based FTS, which provide challenges to surface sciences and analytic techniques.

Acknowledgment: This work was supported by the National Basic Research Program of China (no. 2011CB201406), the National Natural Science Foundation of China (no. 21273262& 21273266), and the Chinese Academy of Science and Synfuels CHINA. Co., Ltd. We also acknowledge general financial support from the BMBF and the state of Mecklenburg-Vorpommern.

Electronic Supplementary Information (ESI) available: Verification of the surface models (Table S1-2); adsorption energies and detailed structure properties of Cu_{1-6} on $Fe_3C(100)$ and $Fe_3C(010)$ surfaces (Table S3-4); Adsorption energies of Cu_n on Fe(110) and $Fe_3C(001)$ surfaces with respect to Cu atom and bulk fcc-Cu energy (Table S5); Various optimized Cu_n (n = 1-7) configuretions on Fe(100) (Fig. S1-4); various optimized Cu_n (n = 2-7) configurations on Fe(111) (Fig. S5-8); various optimized Cu_n (n = 1-7, 13) configurations on the $Fe_3C(010)$ (Fig. S9-16) and $Fe_3C(100)$ (Fig. S17-24). Surface size effect tests on the larger (5×4) Fe(100) and (2×3) $Fe_3C(010)$ surfaces (Fig. S25-26). See DOI: 10.1039/b000000x/

Reference

1 F. Fischer and H. Tropsch, *Brennstoff Chem*., 1923, **4**, 276-285.

2 F. Fischer and H. Tropsch, *Brennstoff Chem*., 1926, **7**, 97-116.

3 R. B. Anderson, The Fischer-Troposch Synthesis, Academic Press, Orlando, FL, 1984, p. 3.

4 N. S. Govender, M. H. J. M. de Croon and J. C. Schouten, *Appl. Catal., A,* 2010, **373**, 81-89.

5 S. Li, W. Ding, G. D. Meitzner and E. Iglesia, *J. Phys. Chem. B,* 2002, **106**, 85-91.

6 B. H. Davis, *Catal. Today,* 2009, **141**, 25-33.

7 F. H. Herbstein, J. Smuts and J. N. van Niekerk, *Anal. Chem.,* 1960, **32**, 20-24.

8 E. de Smit, F. Xinquini, A. M. Beale, O. V. Safonova, W. van Beek, P. Sautet and B. M. Weckhuysen, *J. Am. Chem. Soc.,* 2010, **132**, 14928-14941.

9 T. Herranz, S. Rojas, F.J. Pérez-Alonso, M. Ojeda, P. Terreros and J. L. G. Fierro, *J. Catal*., 2006, **243**, 199-211.

10 P. H. Emmett, Crystallite Phase and Their Relationship to Fischer-Tropsch Catalysis. Reinhold: New York, 1956; p 407.

11 D. Mahajan, P. Gütlich, J. Ensling, K. Pandya, U. Stumm and P. Vijayaraghavan, *Energy Fuels,* 2003, **17**, 1210-1221.

12 A. A. Mirzaei, R. Habipour, M. Faizi and E. Kashi, *Appl. Catal. A,* 2006, **301**, 272-283.

13 E. van Steen and M. Claeys, *Chem. Eng. Technol*. 2008, **31**, 655-666.

14 A. F. H. Wielers, C. E. C. A. Hop, J. van Beijnum, A. M. van der Kraan and J. W. Geus, *J. Catal*., 1990, **121**, 364-374.

15 R. J. O'Brien, L. Xu, R. L. Spicer, S. Bao, D. R. Milburn and B. H. Davis, *Catal. Today,* 1997, **36**, 325-334.

16 E. de Smit, A. M. Beale, S. Nikitenko and B. M. Weckhuysen, *J. Catal.,* 2009, **262**, 244-256.

17 Z. H. Chonco, A. Ferreira, L. Lodya, M. Claeys and E. van Steen, *Catal.,* 2013, **307**, 283-294.

18 Z. H. Chonco, L. Lodya, M. Claeys and E. van Steen, *J. Catal.,* 2013, **308**, 363-373.

19 S. Li, A. Li, S. Krishnamoorthy and E. Iglesia, *Catal. Lett.,* 2001, **77**, 197-205.

20 K. R. P. M. Rao, F. E. Huggins, G. P. Huffman, R. J. Gormley, R. J. O'Brien and B. H. Davis, *Energy & Fuels,* 1996, **10**, 546-551.

21 C. H. Zhang, Y. Yang, B. T. Teng, T. Z. Li, H. Y. Zheng, H. W. Xiang and Y.-W. Li, *J. Catal.,* 2006, **237**, 405-415.

22 R. J. O'Brien and B. H. Davis. *Catal. Lett.* 2004, **94**, 1-6.

23 E. Boellaard, A. M. van der Kraan, A. B. P. Sommen, J. H. B. J. Hoebink, G. B. Marin and J. W. Geus, *Appl. Catal. A,* 1999, **179**, 175-187.

24 H. Hayakawa, H. Tanaka and K. Fujimoto, *Appl. Catal. A,* 2006, **310**, 24-30.

25 D. B. Bukur, D. Mukesh and S. A. Patel, *Ind. Eng. Chem. Res*., 1990, **29**, 194-204.

26 S. L. Soled, E. Iglesia, S. Miseo, B. A. Derites and R. A. Fiato, *Top. Catal*., 1995, **2**, 193-205.

27 I. E. Wachs, D. J. Dwyer and E. Iglesia, *Appl. Catal*., 1984, **12**, 201-217.

28 E. de Smit, F. M. F. de Groot, R. Blume, M. Hävecker, A. Knop-Gericke and B. M. Weckhuysen, *Phys. Chem. Chem. Phys.,* 2010, **12**, 667-680.

29 W. Ma, E. L. Kugler and D. B. Dadyburjor, *Energy & Fuels,* 2011, **25**, 1931-1938.

30 K. Pansanga, N. Lohitharn, A. C. Y. Chien, E. Lotero, J. Panpranot, P. Praserthdam and J. G. Goodwin Jr, *Appl. Catal. A.,* 2007, **332**, 130-137.

31 A. F. H. Wielers, G. W. Koebrugge and J. W. Geus, *J. Catal*. 1990, **121**, 375-385.

32 J. W. Bae, S. J. Park, S. H. Kang, Y. J. Lee, K. W. Jun and Y. W. Rhee, *J. Ind. Eng. Chem*., 2009, **15**, 798-802.

33 M. Kölber H. Ralek, *Catal. Rev.,* 1980, **21**, 225-274.

34 O. Lytken, H. N. Waltenburg and I. Chorkendorff, *Surf. Sci.*, 2003, **543**, 207-218.

35 M. Elahifard, E. Fazeli, A. Joshani and M. Gholami, *Surf. Interface Anal.,* 2013, **45**, 1081-1087.

36 X. H. Zhao, Y.-W. Li, J. Wang and C. F. Huo, *J. Fuel Chem. Technol*., 2011, **39**, 956-960.

37 Y. H. Zhao, S. G. Li and Y. H. Sun, *J. Phys. Chem. C,* 2013, **117**, 24920-24931.

38 X.-X. Tian, T. Wang, Y. Yang, Y.-W. Li, J. Wang and H. Jiao, *J. Phys. Chem. C,* 2014, **118**, 20472–20480.

39 X.-X. Tian, T. Wang, Y. Yang, Y.-W. Li, J. Wang and H. Jiao, *J. Phys. Chem. C,* 2014, **118**, 21963–21974.

40 G. Kresse and J. Furthmüller, *Comput. Mater. Sci.,* 1996, **6**, 15-50.

41 G. Kresse and J. Furthmüller, *Phys. Rev. B,* 1996, **54**, 11169-11186.

42 P. E. Blöchl, *Phys. Rev. B,* 1994, **50**, 17953-17979.

43 J. P. Perdew and Y. Wang, *Phys. Rev. B,* 1992, **45**, 13244-13249.

44 J. P. Perdew, K. Burke and M. Ernzerhof, *Phys. Rev. Lett.* 1996, **77**, 3865-3868.

45 G. Henkelman, A. Arnaldsson and H. Jónsson, *Comput. Mater. Sci.,* 2006, **36**, 354-360.

46 H. Jónsson, G. Mills and K. W. Jacobsen, In Classical and Quantum Dynamics in Condensed Phase Simulations; B. J. Berne, G. Ciccotti and D. F. Coker, Eds.; World Scientific: Singapore, 1998, p385.

47 G. Henkelmann, B. P. Uberuaga and H. Jnsson, *J. Chem. Phys*., 2000, **113**, 9901-9904.

48 J. Blanchard and N. Abatzoglou, *Catal. Today,* 2014, **237**, 150–156.

49 R. Kohlhaas, P. Dunner and N. Schmitzp, Z. *Angew. Phys.,* 1967, **23**, 245-249.

50 C. Kittel, Introduction to Solid State Physics; Willey, New York, 2005.

51 P. Blonski and A. Kiejna, *Surf. Sci*. 2007, **601**, 123-133.

52 C. F. Huo, B. S. Wu, P. Gao, Y. Yang, Y.-W. Li and H. Jiao, *Angew. Chem. Int. Ed*., 2011, **50**, 7403-7406.

53 T. Wang, S. G. Wang, Q. Q. Luo, Y.-W. Li, J. Wang, M. Beller and H. Jiao, *J. Phys. Chem. C,* 2014, **118**, 4181-4188.

54 I. R. Shein, N. I. Medvedeva and A. L. Ivanovskii, *Phys. B -Condensed Matter,* 2006, **371**, 126-132.

55 E. J. Fasiska and G. A. Jeffrey, *Acta Cryst.* 1965, **19**, 463-471.

56 I. N. Shabanova and V. A. Trapeznikov, *JETP Lett.,* 1973, **18**, 339-341.

57 W. C. Chiou Jr. and E. A. Carter, *Surf. Sci.,* 2003, **530**, 87-100.

58 X. Y. Liao, D. B. Cao, S. G. Wang, Z. Y. Ma, Y.-W. Li, J. Wang and H. Jiao, *J. Mol. Catal. A,* 2007, **269**, 169-178.

59 X. Y. Liao, S. G. Wang, Z. Y. Ma, J. Wang, Y.-W. Li and H. Jiao, *J. Mol. Catal. A,* 2008, **292**, 14-20.

60 L. J. Deng, C. F Huo, X. W. Liu, X. H. Zhao, Y.-W. Li, J. Wang and H. Jiao, *J. Phys. Chem. C,* 2010, **114**, 21585–21592.

61 Z. Q. Wang, S. H. Lu, Y. S. Li, F. Jona, P. M. Marcus, *Phys. Rev. B,* 1987, **35**, 9322-9325.

62 B. Heinrich, Z. Celinski, J. F. Cochran, W. B. Muir, J. Rudd, Q. M. Zhong, A. S. Arrott, K. Myrtle and J. Kirschner, *Phys. Rev. Lett.,* 1990, **64**, 673-676.

63 Y. Kamada and M. Matsui, *J. Phys. Soc. Jpn.,* 1997, **66**, 658-663.

64 Guvelioglu, G. H.; Ma, P.; He, X.; Forrey, R. C.; Cheng, H. Evolution of Small Copper Clusters and Dissociative Chemisorption of Hydrogen. *Phys. Rev. Lett.* **2005**, *94*, 026103.

65 Sz Klein, S. Stepanovskyi and J. Śliwiński, *Appl. Surf. Sci.,* 2010, **256**, 4801-4805.

66 D. E. Jiang and E. A. Carter, *Phys. Rev. B,* 2005, **71**, 045402

67 D. C. Sorescu, *Phys. Rev. B,* 2006, **73**, 155420

68 S. Riikonen, A. V. Krasheninnikov and R. M. Nieminen, *Phys. Rev. B*, 2010, **82**, 125459.

69 D. E. Jiang and E. A. Carter, *Phys. Rev. B,* 2003, **67**, 214103.

70 C.A. Wert, *Phys. Rev.,* 1950, **79**, 601.

71 I. R. Shein, N. I. Medvedeva and A. L. Ivanovskii, *Phys. Status Solidi B,* 2007, **244**, 1971-1981.

72 C. K. Ande and M. H. F. Sluiter, *Acta Mater.,* 2010, **58**, 6276-6281.

73 L. C. Allen, *J. Am. Chem. Soc.,* 1989, **111**, 9003-9014.